



Comparison of Single- and Dual-Polarization-Based Rainfall Estimates Using NEXRAD Data for the NASA Iowa Flood Studies Project

BONG-CHUL SEO

IIHR-Hydroscience and Engineering, The University of Iowa, Iowa City, Iowa

BRENDA DOLAN

Department of Atmospheric Science, Colorado State University, Fort Collins, Colorado

WITOLD F. KRAJEWSKI

IIHR-Hydroscience and Engineering, The University of Iowa, Iowa City, Iowa

STEVEN A. RUTLEDGE

Department of Atmospheric Science, Colorado State University, Fort Collins, Colorado

WALTER PETERSEN

Wallops Flight Facility, NASA GSFC, Wallops, Virginia

(Manuscript received 9 September 2014, in final form 18 February 2015)

ABSTRACT

This study compares and evaluates single-polarization (SP)- and dual-polarization (DP)-based radar-rainfall (RR) estimates using NEXRAD data acquired during Iowa Flood Studies (IFloodS), a NASA GPM ground validation field campaign carried out in May–June 2013. The objective of this study is to understand the potential benefit of the DP quantitative precipitation estimation, which selects different rain-rate estimators according to radar-identified precipitation types, and to evaluate RR estimates generated by the recent research SP and DP algorithms. The Iowa Flood Center SP (IFC-SP) and Colorado State University DP (CSU-DP) products are analyzed and assessed using two high-density, high-quality rain gauge networks as ground reference. The CSU-DP algorithm shows superior performance to the IFC-SP algorithm, especially for heavy convective rains. We verify that dynamic changes in the proportion of heavy rain during the convective period are associated with the improved performance of CSU-DP rainfall estimates. For a lighter rain case, the IFC-SP and CSU-DP products are not significantly different in statistical metrics and visual agreement with the rain gauge data. This is because both algorithms use the identical NEXRAD reflectivity–rain rate (Z – R) relation that might lead to substantial underestimation for the presented case.

1. Introduction

During the months of May–June 2013, the National Aeronautics and Space Administration (NASA) conducted a field experiment called Iowa Flood Studies (IFloodS) as part of the Ground Validation (GV)

program for the Global Precipitation Measurement (GPM) mission (see, e.g., Skofronick-Jackson et al. 2013; Hou et al. 2014), carried out in central and northeastern Iowa. The main purpose of IFloodS was to collect high-quality precipitation measurements using a variety of ground-based instruments (including radars with different wavelengths) to assess uncertainties in spaceborne and ground-based estimates of precipitation and impacts of those uncertainties in hydrologic applications and to help characterize the physical process of precipitation production (Petersen and Krajewski 2013). Polarized

Corresponding author address: Bong-Chul Seo, IIHR-Hydroscience and Engineering, The University of Iowa, 100 C. Maxwell Stanley Hydraulics Laboratory, Iowa City, IA 52242.
E-mail: bongchul-seo@uiowa.edu

weather radars were used as the primary instrument for quantitative precipitation estimation (QPE) because, aside from bridging the point estimate of rain gauges to that of a larger satellite footprint, they provide critical information such as size, shape, and concentration of raindrops with high space–time resolution and for the validation of satellite-based precipitation estimates (e.g., Schumacher and Houze 2000; Chandrasekar et al. 2008; Villarini et al. 2009). Therefore, we take this opportunity to focus on the dual-polarization (DP) capability that recently became available to NEXRAD (e.g., Istok et al. 2009) and to assess strengths and weaknesses of DP QPE compared to those of single-polarization (SP) QPE.

A number of radar-rainfall (RR) datasets acquired through IFloodS were extensively evaluated with respect to a scale that is often used for hydrologic applications (Seo et al. 2014). Seo et al. (2014) reveal that the Colorado State University (CSU)-DP estimates generated using the CSU Hydrometeor Identification Rainfall Optimization (CSU-HIDRO; Cifelli et al. 2011) algorithm statistically performs better than radar-only DP estimates (Istok et al. 2009) operationally created by the U.S. National Weather Service (NWS) as well as other SP-based estimates for the IFloodS period. One aspect of the CSU-DP methodology that makes it unique is the three-category hydrometeor identifier that drives the selection of rain-rate estimator based on the precipitation type. The primary goal of this study is to examine in detail the operational aspects of the CSU-DP algorithm related to the precipitation type classification. The CSU-DP algorithm has not been tested in a large scale for NEXRAD because the NWS Radar Operations Center has its own DP algorithm. The hydrometeor identification is an exclusive capability that is relatively hard to achieve in radar-only SP procedures (e.g., Lerach et al. 2010) and is an initial step to define basic features of precipitation. There have been numerous studies to extensively explore hydrometeor identification using dual-polarization radar (e.g., Lim et al. 2005; Park et al. 2009; Chandrasekar et al. 2013) and thus to improve QPE by relating identified information to DP variables such as the differential reflectivity Z_{dr} , specific differential phase K_{dp} , and cross-polar correlation coefficient (e.g., Seliga and Bringi 1976; Sachidananda and Zrnich 1987; Ryzhkov et al. 2005a,b; Giangrande and Ryzhkov 2008). However, there have been few studies (e.g., Cunha et al. 2013) that evaluate operational DP rainfall products applied to the recently upgraded dual-polarization NEXRAD network. Additionally, testing of DP algorithms has been generally limited to research-quality radars. The spatial-resolution difference between current operational ($0.5^\circ \times 250\text{m}$) and earlier polarimetric prototype of

Weather Surveillance Radar-1988 Doppler (WSR-88D) known as the KOUN ($1^\circ \times 250\text{--}267\text{m}$) radar in Oklahoma (see, e.g., Giangrande and Ryzhkov 2008) is another aspect of this study because it might lead to considerable dissimilarity in the outcome of pixel-based rainfall estimation algorithms. In this study, we use the CSU-DP and the Iowa Flood Center (IFC)-SP estimates to evaluate the potential benefit of DP QPE. The same NEXRAD data are used for the generation of the two rainfall estimates. Since the NWS DP product is also evaluated in detail by Cunha et al. (2015), the evaluation of the NWS product is not within the scope of this study.

The study is organized as follows. Section 2 describes the RR estimates used in this study and associated algorithm procedures as well as rain gauge data used as ground reference. Section 3 characterizes three meteorological events selected for the event-based evaluation in which the hydrometeor identification plays a key role in DP QPE. Section 4 evaluates the SP and DP estimates and compares their strengths and weaknesses. In section 5, we discuss the main findings and propose future work.

2. Rainfall data

In this section, we concisely describe the RR products and rain gauge data used in this study. Our RR estimates are generated using the Level II volume data (see, e.g., Kelleher et al. 2007) from NEXRAD that cover the IFloodS study area shown in Fig. 1. The key differences in the structure and specifications between the IFC-SP and CSU-DP processing algorithms are presented and discussed to account for the observed similarities and discrepancies. We use high-quality, dense rain gauge networks that cover the Turkey River basin and the vicinity of the Iowa City area (see Fig. 1) as ground reference to assess the capability of the two RR estimates. The RR estimates and rain gauge data were collected for the period from 1 May to 15 June 2013.

a. IFC-SP product

The Iowa Flood Center provides a real-time composite rain map with the grid spacing of approximately 500 m over the entire state of Iowa for the purpose of flood monitoring and forecasting. This composite rain map is constructed and updated every 5-min based on the reception of the real-time streaming radar Level II volume data using the Unidata Local Data Manager (LDM) and Internet Data Distribution (IDD) technology (e.g., Sherretz and Fulker 1988; Fulker et al. 1997). The downstream LDM in the IFC acquires the Level II data from seven NEXRAD sites that cover Iowa. The acquired radar volume data are processed through

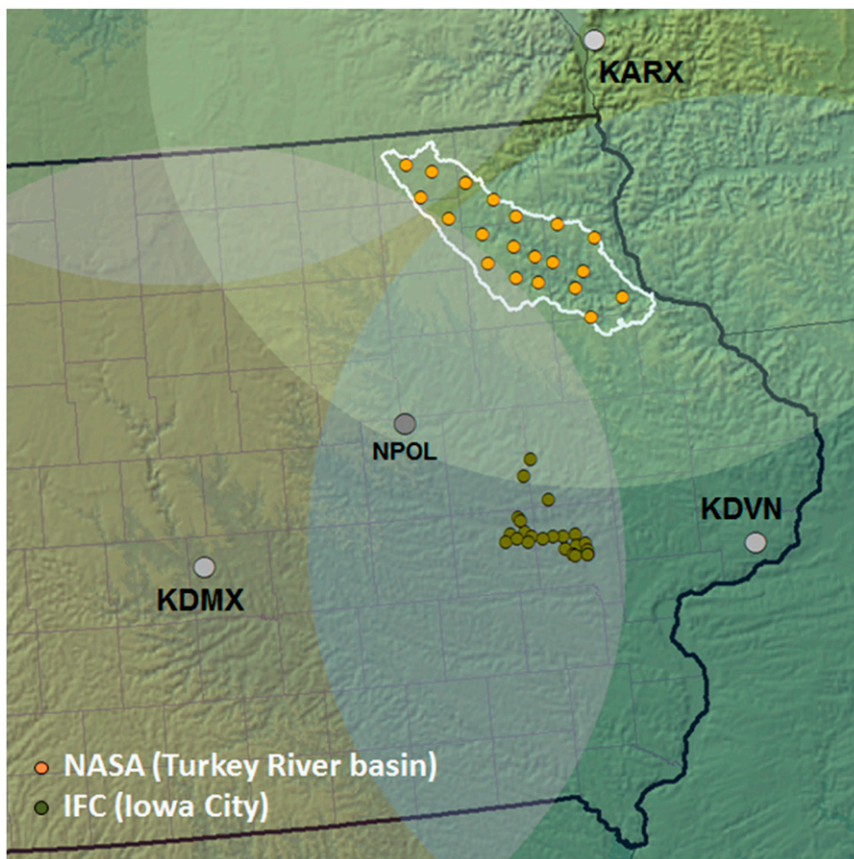


FIG. 1. Study area and two rain gauge networks (NASA and IFC) used as ground reference for the two RR estimates evaluation. The circular domains centered on individual radars indicate 200-km distance from the corresponding radars. The KMPX radar in Minneapolis, Minnesota, is not visible in this domain. The location of NASA's research S-band radar NPOL during the IFloodS campaign is also included for reference.

the Hydro-NEXRAD environment documented in [Krajewski et al. \(2013\)](#) to create the RR estimates. Four NEXRADs that cover the basins of interest are used in this analysis (KARX in La Crosse, Wisconsin; KDMX in Des Moines, Iowa; KDVN in Davenport, Iowa; KMPX in Minneapolis, Minnesota).

In the individual radar data processing of the IFC product, anomalous propagation effects are initially identified and eliminated using three-dimensional structure of the radar reflectivity Z_h data (e.g., [Steiner and Smith 2002](#)) as a quality-control step. The DP variables are not used to classify nonprecipitating radar returns in this SP procedure. The quality-controlled, multielevation-angle data are then used to construct a two-dimensional reflectivity field by using the hybrid scan algorithm detailed in [Seo et al. \(2011\)](#). To synchronize different observation times among individual radars, a simple extrapolation scheme using an advection method (see, e.g., [Krajewski et al. 2013](#)) is applied in

the IFC-SP algorithm. Two consecutive individual reflectivity maps are used to calculate a single-velocity vector for a given time span, and the resulting vector is projected to generate reflectivity maps at the next two 5-min nominal time steps (up to 10 min), assuming that the computed velocity vector will not change in 10 min. The time-synchronized individual maps are merged onto the 500-m common grid based on the exponentially decay weighting scheme with respect to distance from each radar. The statewide reflectivity map is then converted to the rain-rate map by the reflectivity–rain rate (Z – R) relation commonly used for NEXRAD ($Z = 300R^{1.4}$; see, e.g., [Fulton et al. 1998](#)). We note here that the vertical profile of reflectivity (VPR) correction (e.g., [Vignal and Krajewski 2001](#)) is not applied herein because of the high variance of range-dependent errors (e.g., [Krajewski et al. 2011](#)) and possible gross overestimation of rainfall at far range (e.g., [Bellon et al. 2007](#)). For the evaluation in this study, the rain-rate

maps were accumulated over various time scales such as hourly and the entire period.

b. CSU-DP product

For the DP rain-rate product, individual radar data are quality controlled to eliminate nonmeteorological echo using thresholds on dispersion of the differential phase, cross-polar correlation coefficient, and signal to noise ratio (Wang and Chandrasekar 2009). The specific differential phase is calculated using the adaptive methodology of Wang and Chandrasekar (2009). The DP algorithm follows the CSU-HIDRO method of Cifelli et al. (2011) where an appropriate polarimetric rain-rate estimator is selected based on a simple three-category (rain, mix, and ice) Hydrometeor Classification System for Rainfall Estimation (HCS-R), which uses the polarimetric information along with a sounding to determine the water phase within a radar sampling volume. Under all liquid conditions identified by HCS-R, the algorithm attempts to use $R-K_{dp}-Z_{dr}$ or $R-Z_h-Z_{dr}$ both of which better constrain variations in rain rate with drop size distribution compared to $R-Z_h$ estimators. The selection of each estimator is based on a threshold on the polarimetric data to ensure these are above values severely affected by noise [$Z_{dr} \geq 0.5$ dB, $K_{dp} \geq 0.3^\circ \text{ km}^{-1}$, and $Z_h > 38$ dBZ at S band; see Fig. 3 in Cifelli et al. (2011)]. If all of these thresholds are not met, the algorithm defaults to an $R-Z_h$ relation (here, $Z = 300R^{1.4}$). In the presence of a mixture of ice and water determined by HCS-R, the algorithm uses $R-K_{dp}$ given sufficient phase shift ($K_{dp} > 0.3^\circ \text{ km}^{-1}$ and $Z_h > 38$ dBZ) due to the relative insensitivity of K_{dp} to isotropic scatterers such as hail. Otherwise, as in the case of HCS-R all ice, the algorithm does not calculate a rain rate. The implication of this logic is that no rain rate is calculated above the bright band. In other words, at long ranges from the radar when the radar beam is in or above the bright band, the DP method is not applicable. Further discussion of the DP algorithm and the specific equations for each rain-rate estimator are given in Cifelli et al. (2011). We used the same hybrid scan, time synchronization, and merging schemes employed in the SP algorithm for the creation of a composite map from the individual DP rain-rate products.

c. Rain gauge data

High-quality rain gauge data are required to assure the credibility and reliability of the RR product evaluation that is often subject to the accuracy of the ground reference data. In this study, we selected two rain gauge networks, the NASA and IFC (see Fig. 1), which were deployed and operated for IFloodS. During the field campaign, these two networks were regularly

maintained by the IFC staff and students at the University of Iowa. The reported errors and malfunctions were corrected in the postprocessing of the rain gauge data. In the NASA network, 20 rain gauges were deployed in the range between 90 and 130 km from the KARX radar and almost evenly distributed over the Turkey River basin, which enables the investigation of hydrologic impact from inherent uncertainty in the RR estimates as well as the evaluation of the RR itself. The IFC network consists of 30 rain gauges centered on the Iowa City Municipal Airport, including 11 locations within the Clear Creek basin (see, e.g., Villarini et al. 2014). The gauges are located at a range of 80–120 km from the KDVN radar.

Both the NASA and IFC networks are structured with the same configuration of two tipping-bucket gauges at each site. We used the accumulated number of tips data with the time resolution of 5 min. The double tipping-bucket feature reduces the gauge sampling effect due to rainfall variability on a small scale (see, e.g., Ciach 2003) and allows us to detect malfunctioning gauges, such as shown in Fig. 2. In Fig. 2, the disagreement of rain gauge records observed from two rain gauge clusters around Iowa City is presented. We use an arbitrary threshold of 5 mm (for hourly accumulation) to address the observed difference between two tipping buckets in the same rain gauge platform. This threshold value should well represent the systematic measurement errors such as overestimation or undercatch issues (e.g., Steiner et al. 1999) as well as rainfall spatial variability. We take an average of two records if the difference is smaller than the threshold. Otherwise, the bigger value/record is selected to account for the issue of undercatch by one of the tipping buckets.

For radar–gauge comparisons, we use point measurements at rain gauge locations for the collocated radar estimates assuming that rainfall spatial variability is not significant at the employed time (e.g., hourly) and space (0.5 km) scales (e.g., Krajewski et al. 2003; Ciach and Krajewski 2006). We also assume negligible wind effect between the radar sampling height and ground.

d. Precipitation classification

Using the HCS-R output from the DP and the selected rain-rate estimator (e.g., $R-K_{dp}$, $R-K_{dp}-Z_{dr}$, $R-Z_h$, or $R-Z_h-Z_{dr}$), we have devised a precipitation classification to help put the DP and SP statistical performance in context. When the algorithm uses $R-K_{dp}-Z_{dr}$ and HCS-R identifies liquid, the precipitation type is assumed to be heavy rain (HR). If the algorithm identifies liquid but reverts to using an $R-Z_h$ relation, this is indicative of small drops with no appreciable differential signature, and in this regime, these conditions are likely

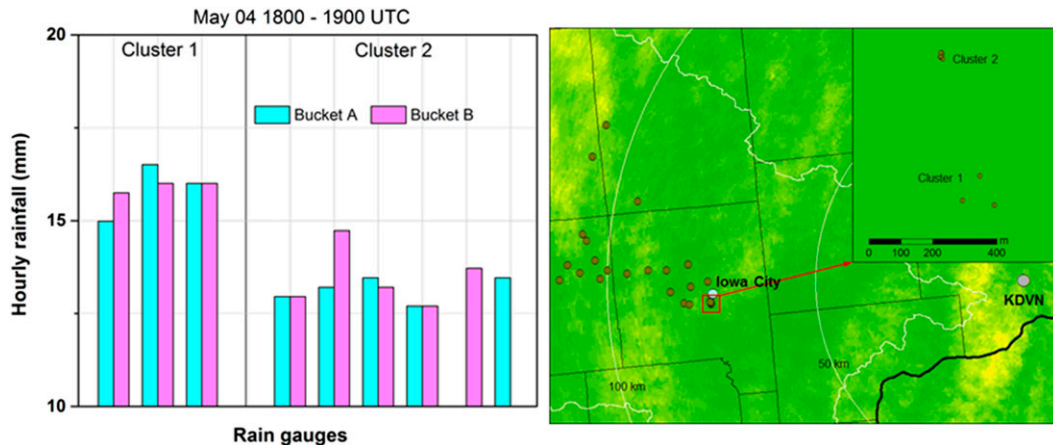


FIG. 2. An example showing rainfall spatial variability at small scale and rain gauge measurement error/difference between two tipping buckets in one location. The two rain gauge locations in cluster 2 indicate that the record for one of the tipping buckets was missed.

light rain (LR). In the case of liquid where $R-Z_h-Z_{dr}$ is selected, reflectivities are generally less than 38 dB (above which the algorithm would try to use $R-K_{dp}-Z_{dr}$ because 38 dBZ is a threshold for using K_{dp} in rainfall estimation at S band), indicative of moderate rain (MR). When $R-K_{dp}$ is used, the HCS-R identification distinguishes whether the point is in the liquid [rain with ice in the liquid phase (RI-L)] or a mix of ice (hail or wet snow) and rain [rain with ice in the mixture (RI-M)]. The HCS-R category of ice (IC) can be associated with wet snow or significant graupel or hail.

3. Meteorological events

The major difference between the SP and DP algorithms is the ability of the DP algorithm to adapt to different precipitation microphysics through the hydrometeor classification and multiparameter rain estimators while the SP algorithm used in this study relies solely on a unique relation between radar reflectivity and rain rate without distinction of storm type or variability in hydrometeor types. To evaluate the estimation performance resulting from the aforementioned algorithm difference, we analyze diverse precipitation cases in May 2013 characterized by different meteorological phenomena. We selected three precipitation cases in which major storms directly affected the two rain gauge networks. We describe meteorological features for the three events in this section. Iowa is relatively flat with some rolling hills, and there are no significant orographic effects (e.g., snow) in the development of precipitation.

The first case (event 1) is identified as a widespread snow/mix and light precipitation event (from 0900 UTC

2 May to 0300 UTC 5 May). In the early morning of 2 May, rain started in a robust southwest-to-northeast-oriented band that moved slowly to the east and transitioned into a rare May snow event in the late morning. The local 1200 UTC DVN sounding in Davenport, Iowa (the location is the same as KDVN shown in Fig. 1) showed multiple freezing levels and elevated conditional instability. Radar echoes were marked with embedded convection. On 3 May, frozen and mixed snow transitioned to stratiform rain between 1300 and 1400 UTC because of the complex melting layer structure and the westward movement of the rain-snow line. There was some convection in a rotating band in south and southeast of the domain shown in Fig. 1 on 4 May. The convection had tops of roughly 6–8 km and generated some heavy rain and lightning. Some isolated cells ahead of the convective line moving northward merged together to create an east-west band of rain.

The other two cases (events 2 and 3) are characterized by mesoscale convective systems (MCSs; from 1000 UTC 19 May to 0700 UTC 20 May and from 1900 UTC 29 May to 0600 UTC 30 May). At the beginning of the event on 19 May, a narrow band of convection developed and passed over the Turkey River basin. A few isolated cells developed to the southwest around 2000 UTC 19 May and then rapidly moved off to the northeast. Shortly after 0000 UTC 20 May, a strong line of convection was observed, moving toward the east from the west. This convective event was quickly followed by the passage of an asymmetric MCS from the southwest, with a strong convective line, well-defined transition zone, and an extensive trailing stratiform region that was enhanced behind the northern part of the line. Overall, heavy rain fell in northern and western Iowa, with

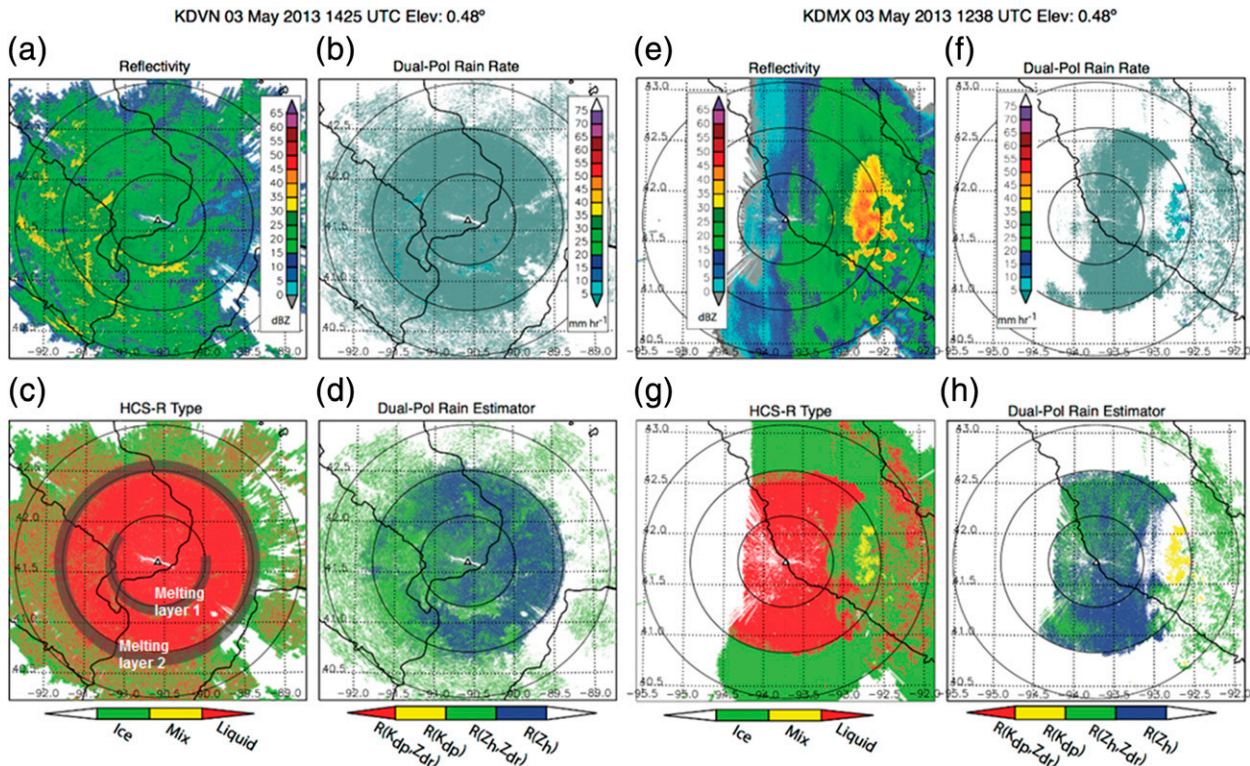


FIG. 3. An overview of the 3 May (event 1) case from (a)–(d) KDVN at 1425 UTC and (e)–(h) KDMX at 1238 UTC. Illustrated is (a),(e) reflectivity; (b),(f) DP rain rate; (c),(g) the three-category HCS-R; and (d),(h) DP rain estimator. Circular rings depict every 50-km range from the radars. Shaded rings in the KDVN HCS-R indicate the locations of two radar-detected melting layers.

corresponding smaller amounts within the Turkey River basin.

On 29 May, some isolated but strong cells merged together and developed into an MCS. The MCS developed to the north and moved to the northeast; as with the 19–20 May case, large portions of the system were followed by widespread stratiform rain.

4. Results

In Figs. 3–5, we provide example snapshots of radar reflectivity, DP rain rate, the three-category HCS-R, and DP rain estimator observed from the KARX, KDMX, and KDVN radars for the three events selected in section 3. The HCS-R maps were generated using the CSU-DP algorithm. We briefly describe event features characterized using the HCS-R maps and how the HCS-R maps are used in estimating rain rate for each event. During the colder, more stratiform case (event 1), the HCS-R classified all liquid and ice, with two distinct freezing levels (Fig. 3). In this relatively light rain regime, the DP rain-rate estimator relies mainly on $R-Z_h-Z_{dr}$ and $R-Z_h$ since K_{dp} values were not large enough to provide meaningful constraints on the rain-rate

estimates. In the more convective events 2 and 3 (19–20 May and 29–30 May), the DP rain estimation method optimized the use of the information provided by the polarimetric observations (Figs. 4, 5). The HCS-R identified areas of mixed rain and hail in the convective cores, and the algorithm subsequently relies on $R-K_{dp}$ to estimate rain rate under those conditions since K_{dp} is insensitive to isotropic scatterers such as hail that render the power-based measurements of reflectivity and differential reflectivity less useful. The more intense cases also allowed for the algorithm to use information from both K_{dp} and Z_{dr} via the $R-K_{dp}-Z_{dr}$ relation and only defaulted to the $R-Z_h$ estimator in the very light rain regions around the edges of the storms (Figs. 4, 5).

a. Event totals

We illustrate maps of total rainfall for the selected three events in Fig. 6 [IFC-SP in Fig. 6 (left) and CSU-DP in Fig. 6 (right)]. Event 1 in Figs. 6a and 6b shows relatively less rainfall than the other two events because it is characterized by snow/mix and stratiform types of precipitation (see section 3). The major difference noticeable between Figs. 6a and 6b is a region around the KDMX radar. While reflectivity remained relatively

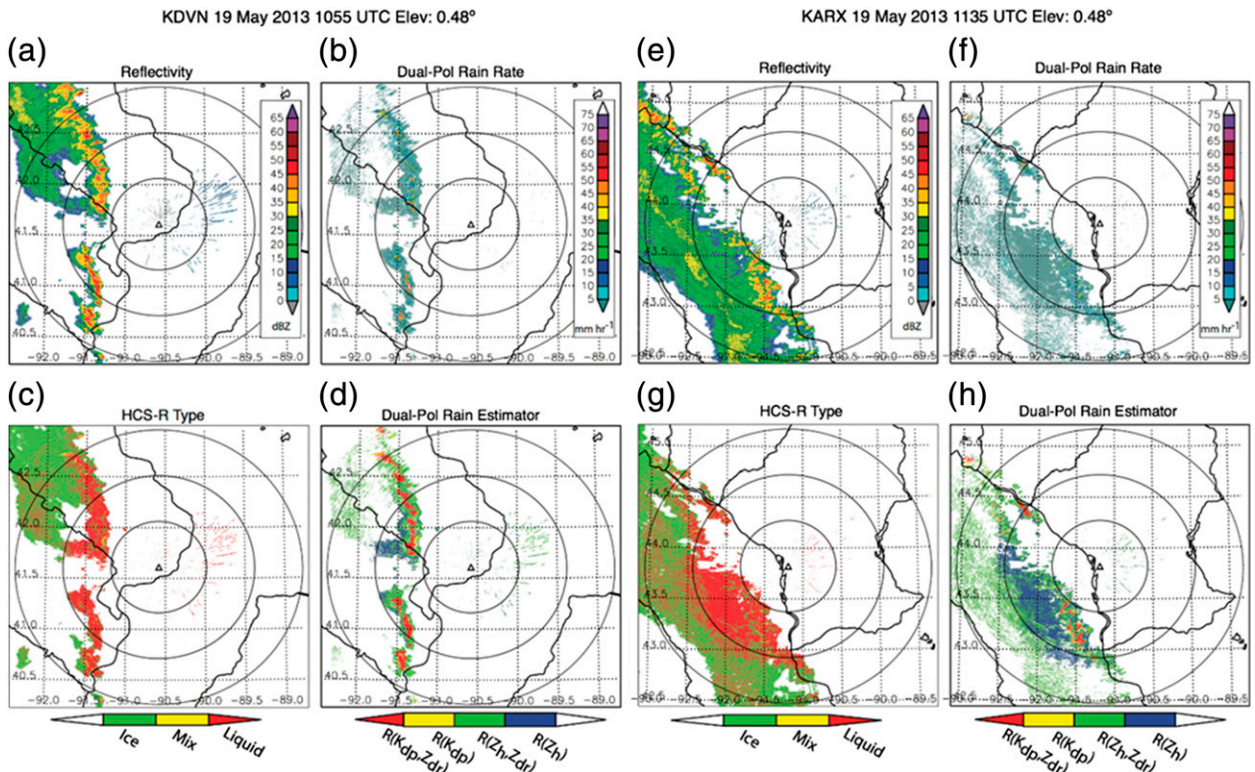


FIG. 4. An overview of the 19 May (event 2) case from (a)–(d) KDVN at 1055 UTC and (e)–(h) KARX at 1135 UTC. Illustrated is (a),(e) reflectivity; (b),(f) DP rain rate; (c),(g) the three-category HCS-R; and (d),(h) DP rain estimator. Circular rings depict every 50-km range from the radars.

strong (up to 50 dBZ) during this rain–snow mix, the DP HCS-R detects the presence of cold precipitation even at close range (see the KDMX snapshots in Fig. 3). This is because of robust polarimetric signatures associated with melting, such as a lowering of correlation coefficient. The mixed-phase nature and low melting level associated with this case are manifest as a range limit in Fig. 6. Based on the WSR-88D volume coverage patterns, the radar beam (center) altitude of the lowest elevation angle (0.5°) is around 2 km at 120-km range, and radar measurements of the lowest elevation angle at far range used to be affected by the low melting layer. These range effects in the CSU-DP, however, are not visible in the cases of events 2 and 3 (Figs. 6d,f) for which a vertically well-developed and well-mixed convective structure played a major role for storm creation, and the melting layer was much higher during those cases, at a height of 3.5–4.0 km. While both the IFC and NASA network locations shown in Fig. 6 accumulated some amounts of rainfall in event 1, the IFC locations in events 2 and 3 do not show meaningful rainfall in both RR event totals. Therefore, we use both rain gauge networks for event 1 and only the NASA (Turkey River)

network for events 2 and 3 to compare and evaluate the two RR products in this section.

In Table 1, we provide two simple rainfall statistics for each event case, namely, mean areal rainfall (precipitation) and maximum hourly accumulation. The mean areal rainfall is identified as the mean of event totals at corresponding RR grid pixels with rain gauge locations. Overall, the estimated rainfall in the CSU-DP tends to be slightly closer to the rain gauge observations, although both RR products show underestimation. This underestimation tends to be more significant for the lighter rain case of event 1, where the radar totals are almost half of the gauge totals. The larger gauge value of mean areal rainfall (81.5 mm) at the IFC network in event 1 was due to the relatively longer duration (even if the event is identified as snow/mix and stratiform case that is a less strong precipitation type), and we also note convective activity over the IFC network region at the end of the period resulting in almost twice the rain accumulation compared to the NASA network. The maximum hourly accumulation values in Table 1 demonstrate how intense the rain was in each case, and we recognize that event 3 was the most intense, whereas

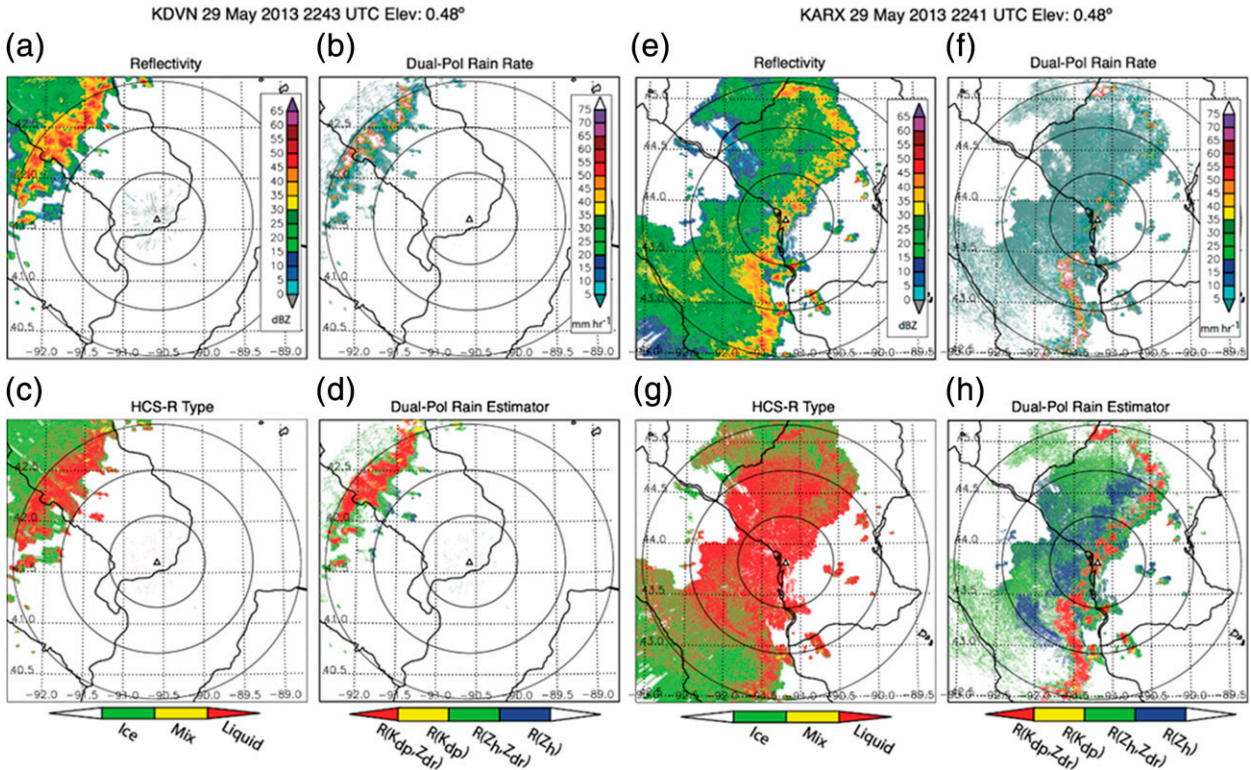


FIG. 5. An overview of the 29 May (event 3) case from (a)–(d) KDVN at 2243 UTC and (e)–(h) KARX at 2241 UTC. Illustrated is (a),(e) reflectivity; (b),(f) DP rain rate; (c),(g) the three-category HCS-R; and (d),(h) DP rain estimator. Circular rings depict every 50-km range from the radars.

event 1 was relatively mild, especially over the NASA gauge locations.

b. Radar–gauge comparison

The hourly radar–gauge comparison results for the events listed in Table 1 are presented in Fig. 7. Figures 7a (left, middle) and 7b (left, middle) are relevant to event 1, and the results from different rain gauge networks are distinguished by different colors of dots. The results for events 2 and 3 are placed in Figs. 7c (left, middle) and 7d (left, middle). The insets in Fig. 7 (left, middle) indicate representative hours in which the two RR estimates showed considerable differences. We use three statistical metrics, namely, multiplicative bias (radar/gauge), correlation coefficient, and root-mean-square error (RMSE) to assess radar–gauge agreement of the two RR estimates. The bias values greater and smaller than one indicate over- and underestimation, respectively. Figure 7 (right) illustrates precipitation type occurrence rate (%) for the inset hours. The occurrence rate is computed for the spatial area of corresponding rain gauge network that can be defined using the ranges of azimuth from the north (0°) and of distance from the radar. For example, the NASA network area

from the KARX radar is defined as 179° – 243° azimuth and 89–132-km distance. The polar-based HSC-R maps at the lowest elevation are then accumulated over inset hours in Fig. 7 for the azimuth and distance ranges.

For Figs. 7a and 7b, the two network areas were likely affected by different types of precipitation, the northern NASA network being influenced by more rain–snow mix and the southern IFC network by heavier convection. The resulting scatter patterns are completely different, although bias values are in similar range. While radar–gauge agreement for the IFC network area shows some improvement in the CSU-DP estimates, the SP and DP estimates for the NASA network do not show much difference, and the improvement in the CSU-DP is little if any. As discussed earlier, some convective storms passed over the IFC network area at the end of the period (event 1), and we find a nonzero occurrence of heavy precipitation beginning just after 1830 UTC. In addition, since the total occurrence rate of all precipitation types is less than 50% during the hours shown, we can infer that the precipitation system was narrow in spatial extent and did not cover the entire domain. On the other hand, for the NASA network area (event 1), we recognize that the precipitation system widely

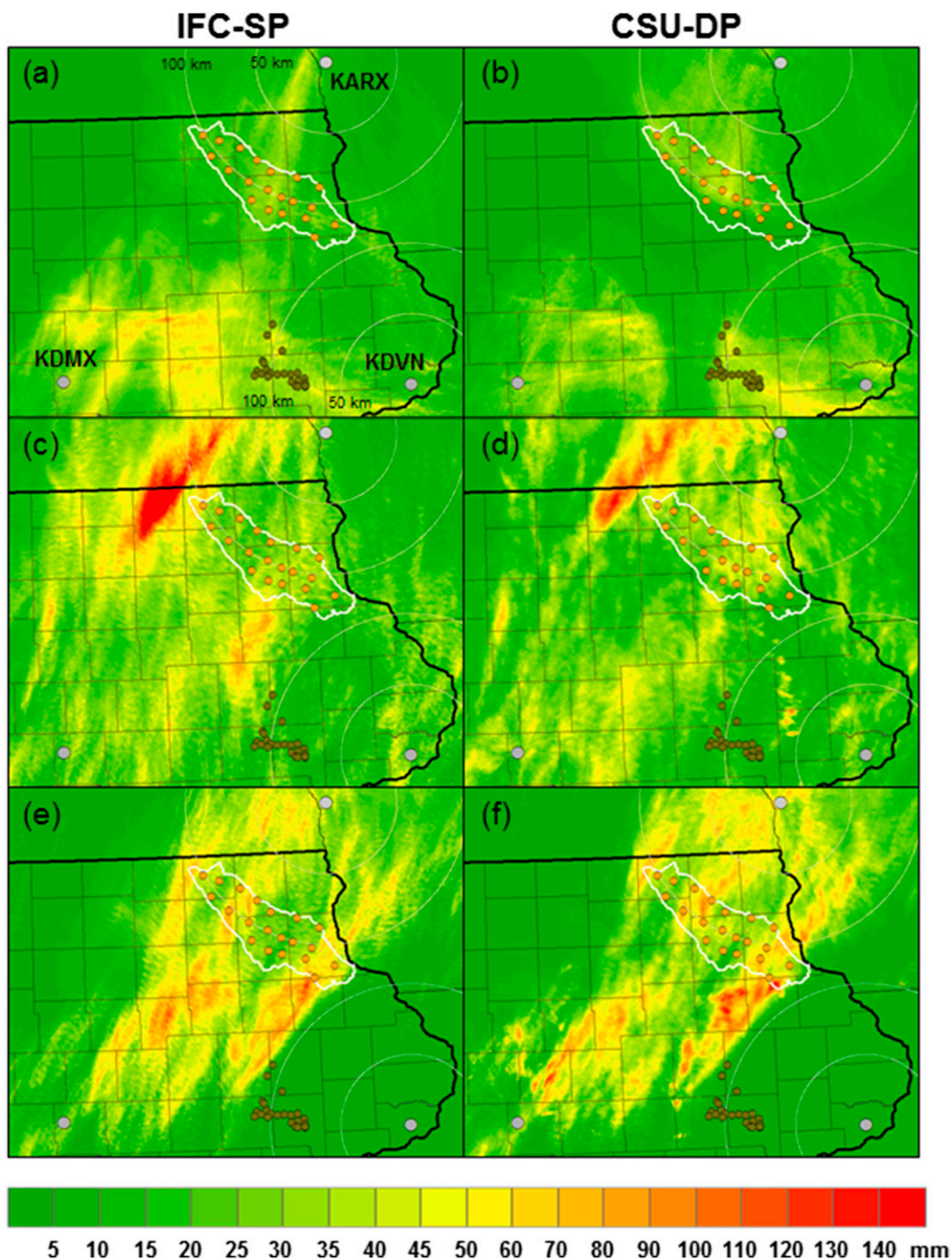


FIG. 6. Event rain total maps for the selected rain cases: (a),(b) event 1; (c),(d) event 2; and (e),(f) event 3. The IFC-SP and CSU-DP are presented (left) and (right), respectively.

covered the area (the Turkey River basin) with almost 100% of total occurrence rate, including about 10% ice (e.g., dry snow) proportion. Here, the bias, correlation, and RMSE are similar between the SP and DP algorithms. Not unexpectedly, this implies that QPE for a

snow/mix or widespread stratiform system with a very low melting layer might be still a challenge even for DP radars based on the presented performance of the CSU-DP for the case of event 1 with the NASA network [Fig. 7b (middle)]. Regarding the cases of events 2 and 3

TABLE 1. Rainfall statistics for the selected three rain cases. The mean areal rainfall for the RR estimates is the mean of event totals at collocated grid pixels with rain gauge locations.

	Gauge network	Mean areal rainfall (mm)			Max hourly accumulation (mm)		
		IFC-SP (radar/gauge)	CSU-DP (radar/gauge)	Gauge	IFC-SP	CSU-DP	Gauge
Event 1	IFC	36.2 (0.44)	39.4 (0.48)	81.5	10.5	12.2	16.3
	NASA	22.0 (0.44)	23.3 (0.47)	49.5	10.5	8.7	8.6
Event 2	NASA	31.2 (0.91)	32.3 (0.94)	34.3	28.1	32.5	29.5
Event 3	NASA	36.4 (0.72)	41.6 (0.83)	50.3	43.8	50.0	44.0

shown in Figs. 7c (right) and 7d (right), the precipitation type occurrence rate reveals some steady proportion of heavy rain accompanying ice or hail particles, which is an indication of convection. The CSU-DP estimates show superior performance in all statistical metrics as well as a visual agreement for these convective cases. The shown enhancement in the CSU-DP is accomplished by the rain-rate estimation using dual-polarimetric variables. For light rain, the IFC-SP and CSU-DP use the same $Z-R$ equation, but rain rate for heavy (DP employs both K_{dp} and Z_{dr}) and moderate rain (where DP uses Z_h and Z_{dr}) can generate significant differences. This is demonstrated in the convective cases shown Figs. 7c and 7d.

c. Time series analysis

To explore dynamic changes in the performance of the SP and DP estimates associated with the variation of precipitation types, the time series of hourly based multiplicative bias and correlation as well as of precipitation type occurrence rate are presented in Figs. 8 and 9. The cases of events 1 (Fig. 8) and 3 (Fig. 9) both with the NASA rain gauge locations are chosen to examine the worst and best cases for RR shown in Fig. 7. For the efficient presentation of the RR performance along the time line, the bias and correlation values are categorized into several classes and color coded according to the defined intervals. For example, blue and red colors represent under- and overestimation for bias, respectively. Likewise, lighter and darker tones indicate each better and worse performance. We used two arbitrary thresholds, hourly minimum rainfall (0.5 mm for both hourly radar and gauge values), and minimum number of available radar-gauge pairs (5) to estimate hourly bias and correlation values. This is because occasionally some spurious rainfall values in a very small number of radar-gauge samples within an hourly interval affect the systematic structure of RR error. The unoccupied time spans in Figs. 8 and 9 indicate that there were an insufficient number of radar-gauge pairs whose rainfall values were greater than the threshold of 0.5 mm. In Fig. 8, we recognize that the proportion of

moderate rain plays an important role in producing meaningful amounts of rainfall because the periods dominated by light rain are times that did not meet the threshold criteria. Interestingly, during the 0200 UTC time period, both CSU-DP and IFC-SP are biased high. This time saw a spike in precipitation identified as IC, with mostly light rain and some moderate rain. The significant underestimation by both SP and DP at the end of the period in Fig. 8 seems to be the result of an increasing contribution from rain and ice mixes. Another possible reason for the underestimation at the end of the time period could be attributed to the conventional $Z-R$ relation that is used not only in the SP algorithm but also in the DP algorithm for light rain. Since the conventional $Z-R$ equation is known to be inappropriate for stratiform-type storms (see, e.g., Klazura and Kelly 1995), the comparable proportion of light rain to that of moderate rain at the end of the period in Fig. 8 might lead to significant underestimation. Interestingly, the SP rainfall is negatively correlated with the rain gauge observations at the end of the period. The considerable portion of ice detected at the times of negative correlation seems to decrease the reliability of the SP estimates. For event 3 (Fig. 9), the CSU-DP clearly shows superior performance in both bias and correlation than the IFC-SP. The contribution of heavy rain is apparent in this convective case and illustrates the tendency for DP estimates to improve as the proportion of moderate to heavy rain increases. Additionally, in this time period some amount of rain-ice mixture was identified, which could indicate contamination from hail, biasing the SP RR. Toward the end of the period when most of the rain is moderate or light, the DP slightly overestimates (bias of 1.07) the rainfall while the SP significantly underestimates (bias of 0.4). In the correlation comparison of Fig. 9, the categorical presentation seems to conceal which one performs better, but actual correlation values at each time step confirm that the correlation values of the CSU-DP are superior to those of the IFC-SP in the same color zone (e.g., 0.93 versus 0.83 for 2300 UTC 29 May).

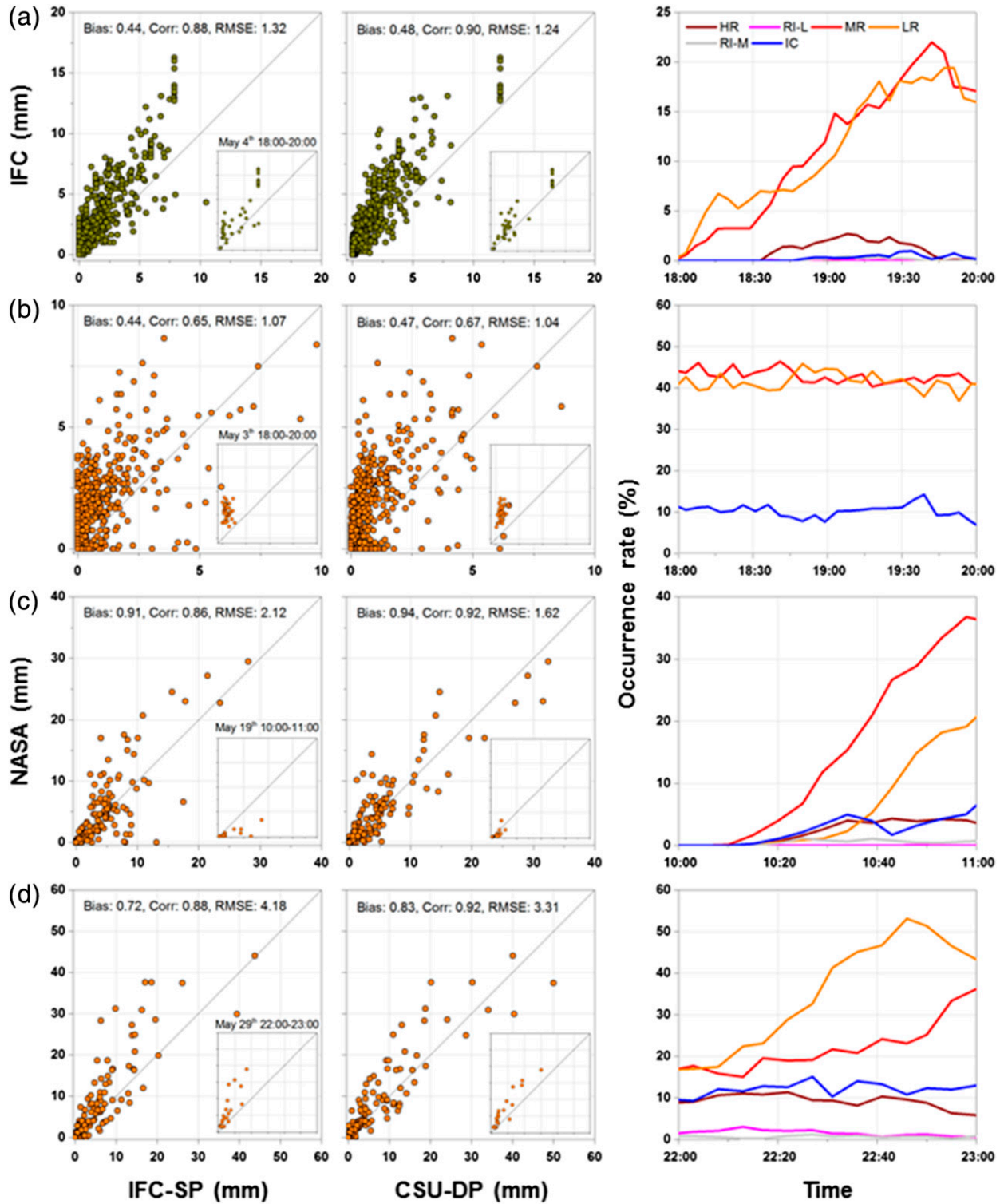


FIG. 7. (left),(middle) Hourly radar–gauge comparison for event 1 with the IFC (a) and NASA rain gauge networks (b), event 2 with the NASA network (c), and event 3 with the NASA network (d). The insets show radar–gauge scatter at the representative hours in each event. (right) The representative hours are used for representing precipitation type occurrence rate over the network areas.

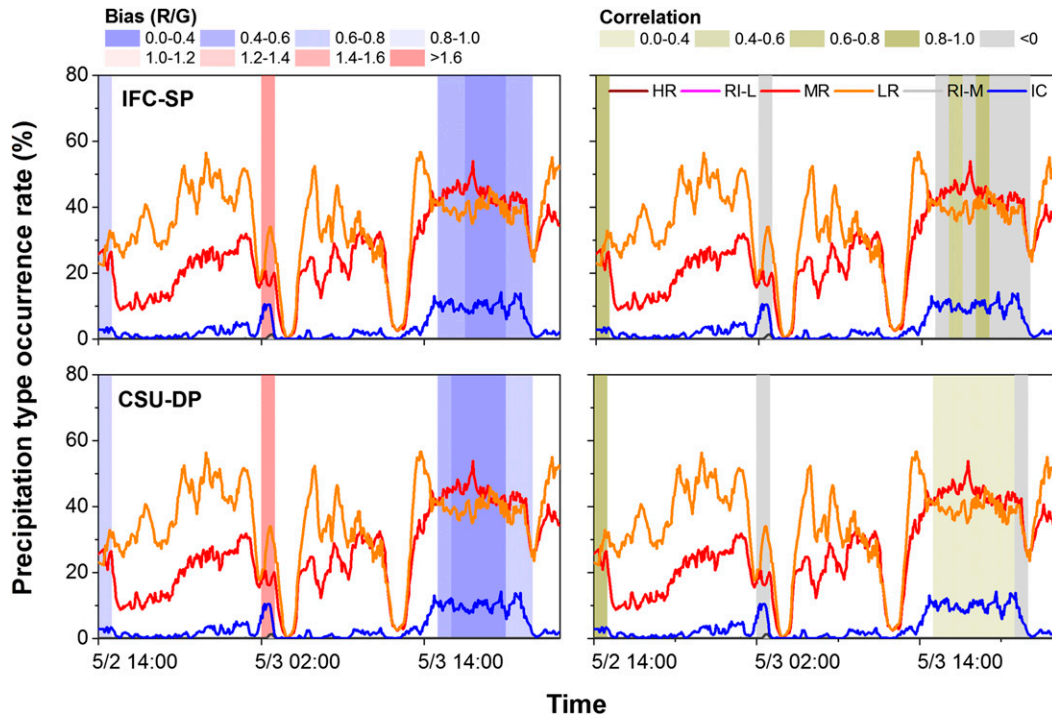


FIG. 8. Precipitation type changes over time for event 1 with the NASA network area. The estimated hourly bias and correlation values are color coded and represented at corresponding time spans.

d. Campaign totals

We now turn to larger spatial and temporal scales to look at how the algorithms performed during the entire IFloodS campaign. The RR maps of total accumulation over the entire campaign period (from 1 May to 15 June) are presented in Fig. 10. The estimated rainfall was up to 500 mm in some regions. On average, the campaign period was wetter than expected in normal years, compared to climatological precipitation in May and June in Iowa (see, e.g., www.prism.oregonstate.edu/normals/). Because of DP nonestimation above the melting level, it is clear that the most striking difference between SP and DP is the limited totals at far ranges from the radars. In examining the rate of occurrence of each precipitation type as a function of range throughout the entire period (Fig. 11), it is clear that, on average, beyond 120 km the contribution from ice systematically increases with range, with a secondary jump at around 145 km. This is due to the behavior of the refractive index of air with height and Earth curvature, which causes the beam to intersect the melting layer at far ranges, and as such the HCS-R identifies a mix of ice or ice particles. The top of the radar beam would start interacting with a mean melting layer (e.g., 3.5 km calculated from the DVN soundings for the campaign period) at the first zone

(110–120 km), and the center of the beam would intersect with the melting layer at the second zone (140–150 km). Once the radar beam is partially or completely in the mixed phase or ice regions, calculation of a surface-based rain rate is not possible with current knowledge of rain microphysics and polarimetric radar. In fact, SP techniques can have similar limitations in and above the bright band, which can result in over- or underestimation of surface rainfall (e.g., Krajewski et al. 2011). We will further discuss the implications for operational rainfall estimation in section 5. For reference, we highlight the rain gauge distance bands from the corresponding radars (KARX-NASA and KDVN-IFC) in Fig. 11. Figures 10 and 11 also demonstrate that the KDMX area was affected by more intense rainfall [heavy and moderate rain in Fig. 11 (middle)] than other areas and that the KDVN area was associated with relatively less rainfall.

The radar–gauge comparison for the rain totals is presented in Fig. 12. Overall, both RR estimates show underestimation against the rain gauge observations. For the Turkey River basin area, the CSU-DP tends to reduce the underestimation tendency observed in the IFC-SP and increase rainfall estimations in most locations. However, six rain gauges that are located at a relatively far range shown in the inset of Fig. 12 (right)

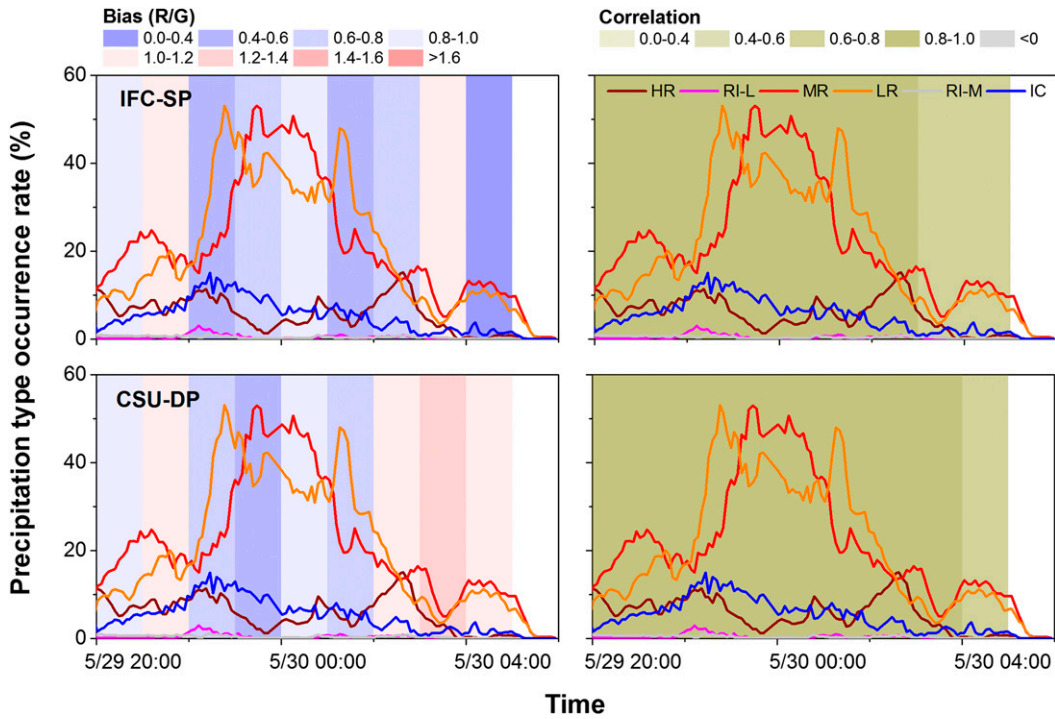


FIG. 9. Precipitation type changes over time for event 3 with the NASA network area. The estimated hourly bias and correlation values are color coded and represented at corresponding time spans.

are associated with significant underestimation (red circle in Fig. 12). This considerable error can be interpreted by the comparatively higher frequency of ice presence at the highlighted range in Fig. 11 (top;

KARX). The rainfall increase in other gauge locations is likely attributed to the proportion of moderate rain for which the CSU-DP algorithm uses Z_h and Z_{dr} as rain-rate estimators because both IFC-SP and CSU-DP

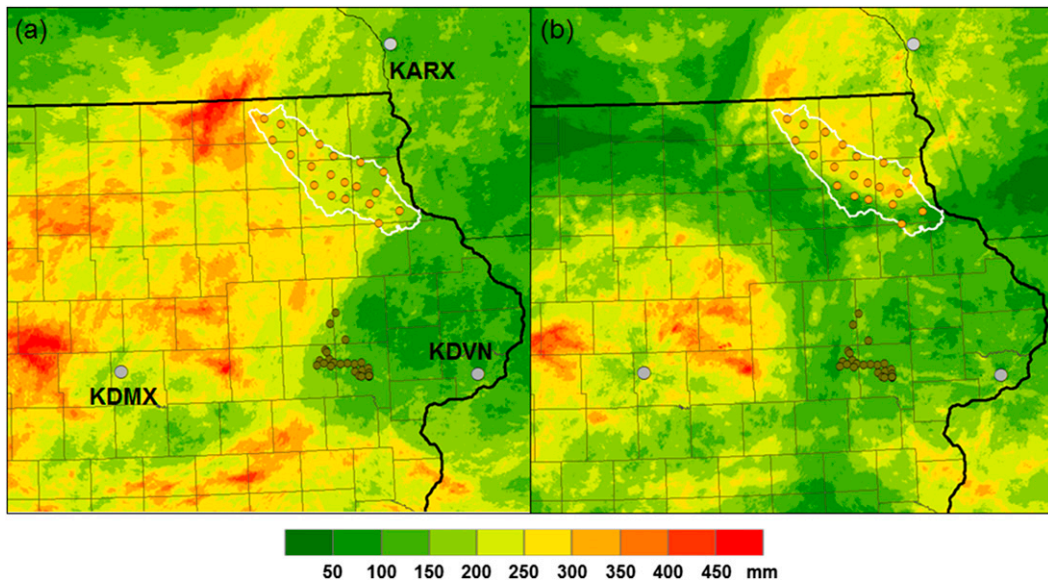


FIG. 10. Rain total maps of the (a) IFC-SP and (b) CSU-DP estimates accumulated over the entire campaign period. The IFC rain gauge network is located in the west of the KDVN radar, and the NASA network is evenly distributed over the marked basin (Turkey River basin) boundary in the southwest of the KARX radar.

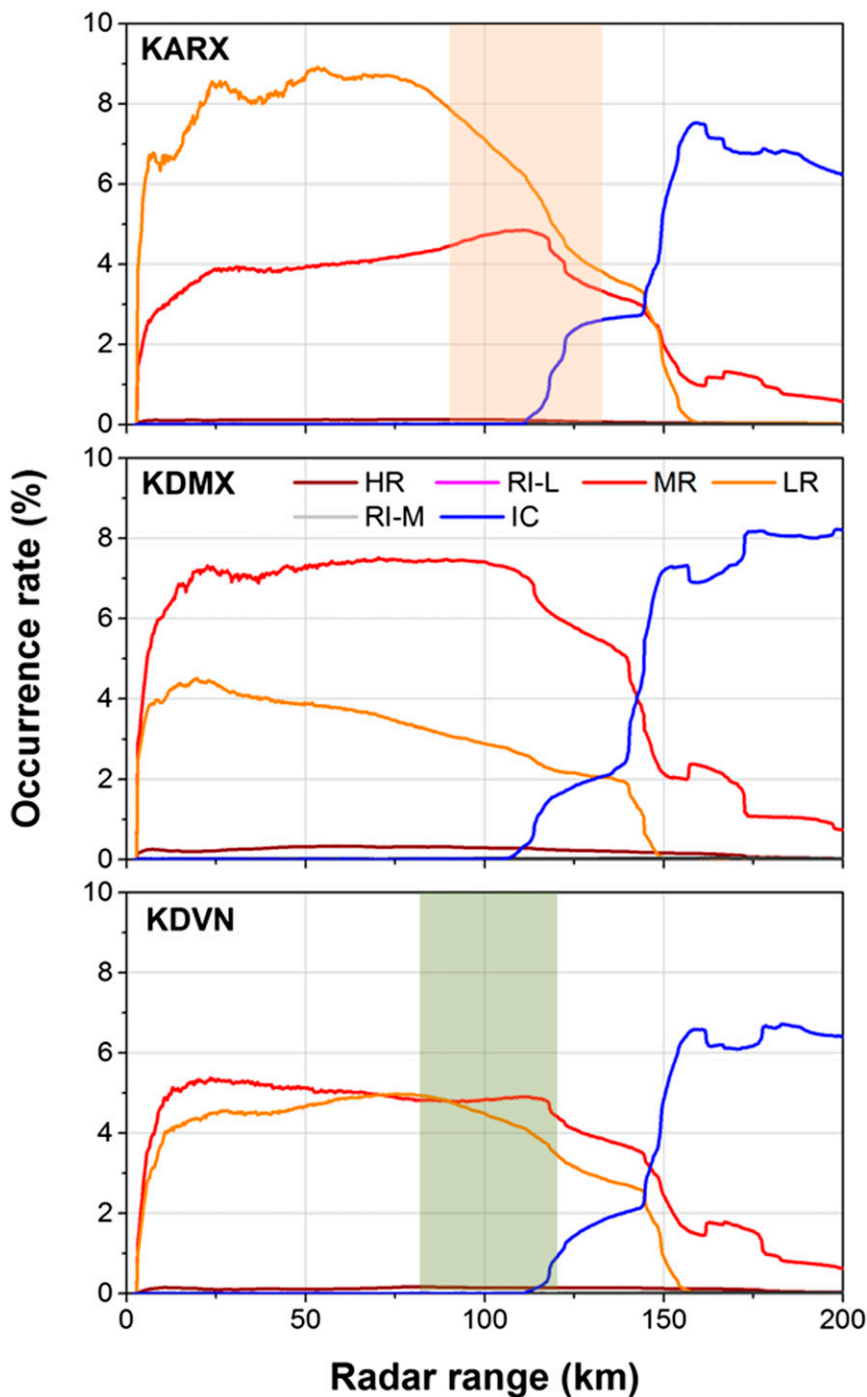


FIG. 11. Occurrence rate of precipitation types over the campaign period with respect to radar range. The shaded range zones for the KARX and KDVN radars indicate the NASA and IFC rain gauge network locations from corresponding radars (KARX-NASA and KDVN-IFC).

algorithms use the same $Z-R$ transformation equation for light rain. Regarding the IFC network, the underestimation for the CSU-DP looks worse than that for the IFC-SP. We further investigated this issue and

identified gauge locations where the CSU-DP estimates are smaller than those of the IFC-SP. We then found that the smaller estimation arose from rain gauge clusters mostly located in the north and west of the network

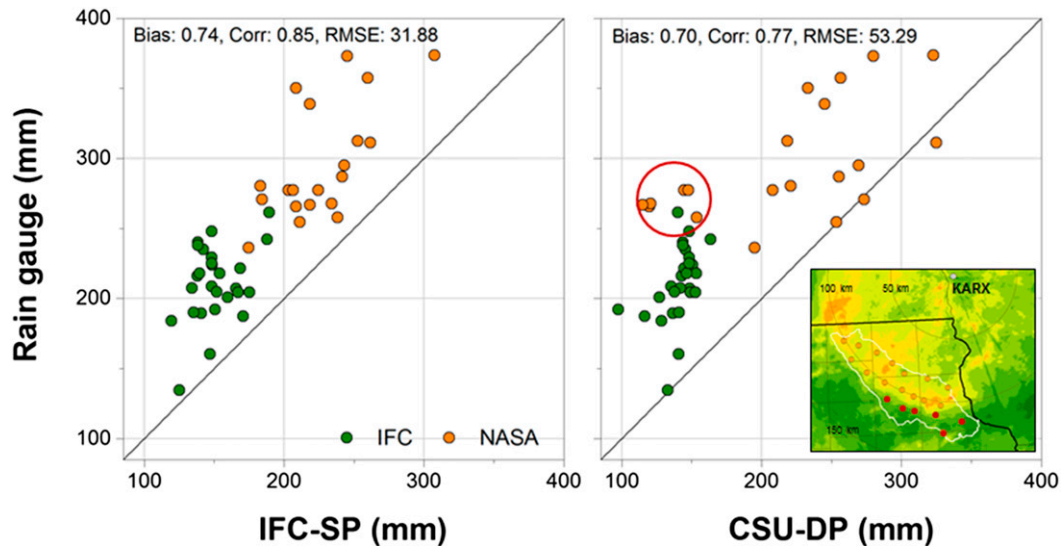


FIG. 12. Radar-gauge comparison for the campaign rain totals of the (left) IFC-SP and (right) CSU-DP estimates. The map of rain total for the CSU-DP is presented in the inset (right) to demonstrate that the significant underestimation (six rain gauge locations within the red circle and these locations are indicated in the map) was caused by the observed range issue. The statistical metric values of multiplicative bias (radar/gauge), correlation coefficient, and RMSE are provided for both estimates.

(see Fig. 1). These several gauges are all located in a 110–120-km range from the KDVN radar, and the ice presence at that narrow range [Fig. 11 (bottom)] might affect the observed consequence in the CSU-DP estimates.

Figure 13 shows the hourly radar-gauge comparison result over the entire period. In Fig. 13, both RR estimates show underestimation of similar magnitude as evidenced by the bias values. The agreement in terms of scatter and liner dependency measured by the RMSE and correlation is better in the CSU-DP than in the IFC-SP. Since most points are congregated in Fig. 13 in the low rainfall totals (e.g., smaller than 5 mm), which may have a larger impact on characterizing the RR error structure, we present a detailed data distribution for the smaller rain area (0–20 mm) with two-dimensional radar-gauge histograms in Fig. 13. Each color used in the two-dimensional histograms represents the data occurrence frequency for given radar-gauge pairs.

5. Discussion and future work

Herein we have examined two different radar-rainfall (RR) algorithms, IFC-SP and CSU-DP, and compared error statistics (bias, correlation, and RMSE) against extensive ground-based rain gauge measurements. Earlier studies (e.g., Brandes et al. 2002; Ryzhkov et al. 2005a,b; Giangrande and Ryzhkov 2008; Cifelli et al. 2011) made advances in testing polarimetric rain-rate

estimators (e.g., $R-Z_h-Z_{dr}$ and $R-Z_h-K_{dp}-Z_{dr}$) and finding/selecting the “best” estimator depending on the echo classification. In this study, we focus on investigating and evaluating the performance of the selected estimators for operational applications. We clearly show likely improvements and limitations in DP estimates depending on the precipitation types. In general, the DP algorithm performed better than the SP across a variety of time scales, from hourly to event and campaign rainfall totals. This is due to the ability of the DP algorithm to “adapt” to the microphysics by using different polarimetric information to constrain the rain estimates. Event-based analysis shows that the CSU-DP is especially advantageous under intense rain. Time series analysis reveals that the change in the proportion of heavy rain plays a significant role for the estimation accuracy because the CSU-DP estimates tend to be fairly close to the rain gauge values when the proportion of heavy rain increases and reaches local peaks, likely because the DP algorithm is able to rely on both K_{dp} and Z_{dr} . However, under light rain and cold conditions, the DP algorithm did not provide any advantage over the SP, as the polarimetric variables were mostly below threshold values, reverting to both algorithms using the same $Z-R$ relation. We think that this weakness in both the DP and SP algorithms can be supplemented to some degree by replacing the current $Z-R$ with one that better represents lighter rain regimes (e.g., Marshall-Palmer $Z-R$; Marshall and Palmer 1948). Additionally, from the

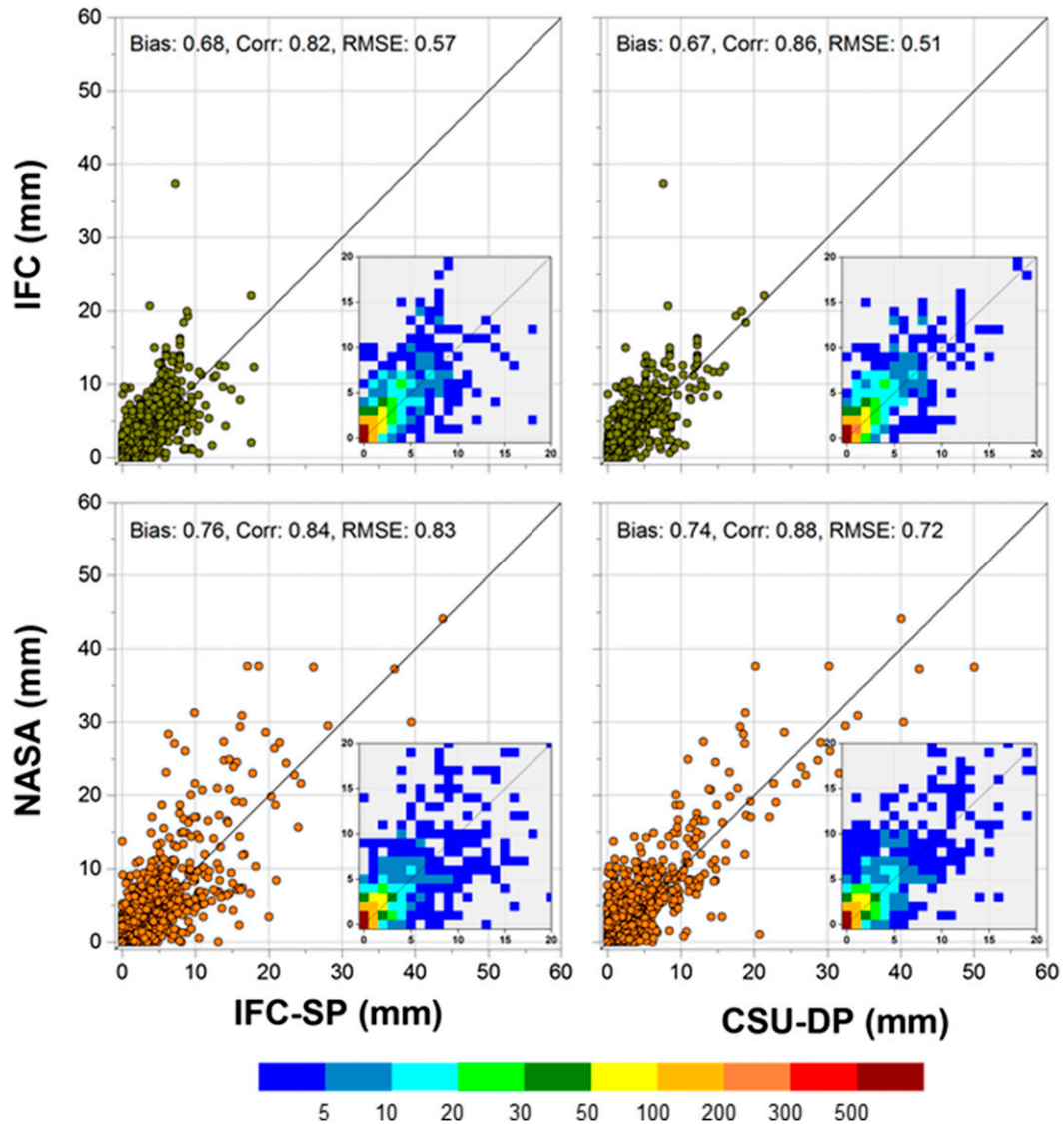


FIG. 13. Hourly radar–gauge comparison result with the statistical metric values of multiplicative bias (radar/gauge), correlation coefficient, and RMSE. The 2D histograms in the insets show data frequency for given radar–gauge pairs.

comparison of radar–gauge rain totals over the entire campaign period, it was found that both IFC-SP and CSU-DP estimates are biased low. The CSU-DP tends to increase the totals at some locations that are positioned within the DP retrieval range, compared to the IFC-SP.

We note that the rain-rate estimators (e.g., $R-Z_h-Z_{dr}$ and $R-K_{dp}-Z_{dr}$) that use Z_{dr} and Z_h might be vulnerable to the radar calibration errors. We performed some spot checking of the Z_{dr} bias using high-elevation angle data in some stratiform cases. We also confirmed with the Radar Operations Center that the Z_{dr} biases of the involved radars for the campaign period were within an

acceptable range (e.g., ± 0.2 dB), and a relative reflectivity calibration among the radars was ± 1 dBZ. This small relative calibration bias can be verified by the fact that rain totals created using reflectivity data (IFC-SP) do not show any sharp border among the radars (see Fig. 10a). However, the absolute calibration is more challenging and could yield errors in the radar-based rainfall estimates (see, e.g., Seo et al. 2013). We hope that the new Dual-Frequency Precipitation Radar (DPR) that was recently launched by GPM can help in resolving the absolute radar calibration issue.

One drawback of the DP algorithm is shown to be the areal extent to which the DP is applicable, which is

limited to regions where the radar beam remains below the melting layer. Although the DP algorithm is found to be more accurate compared to gauge estimates of rainfall, the radar-range limitation is a major problem for applying such an algorithm operationally, where complete spatial coverage is essential for producing streamflow and flood forecasts, for example. The polarimetric algorithm could be significantly improved because it can well detect snow/ice and the location of the melting layer. However, much research still remains to enable such an improvement in the quantitative estimation. Relating polarimetric observations of ice and mixed-phase volumes to surface-based rainfall remains an open research question, but limits the applicability of the DP method in the cold season and at long ranges from the radar in the warm season. We do not expect that a simple application of some dubious $R-Z_h$ estimators proposed for the melting layer or snow/ice regimes would improve the results. One possible solution would be to use a vertical profile of reflectivity (VPR) at far ranges to supplement the DP rainfall analysis.

Acknowledgments. This study was supported by NASA Iowa Flood Studies collaborating with the Iowa Flood Center. The National Science Foundation provided partial support under Award EAR-1327830. The authors are grateful to Daniel Ceynar, James Niemeier, and volunteer students who contributed to the operation of rain gauge networks in Iowa City and the Turkey River basin. We thank Prof. V. Chandrasekar for providing the software for K_{dp} calculation and HCS-R. We would also like to thank Jeffrey Cunningham at the Radar Operations Center for assisting with NEXRAD calibration assessment and Paul Hein at Colorado State University for his help with processing the large amount of NEXRAD data. The authors are grateful to the PMM/GPM Program Management for their support of IFloodS and this research.

REFERENCES

- Bellon, A., G. W. Lee, A. Kilambi, and I. Zawadzki, 2007: Real-time comparisons of VPR-corrected daily rainfall estimates with a gauge Mesonet. *J. Appl. Meteor. Climatol.*, **46**, 726–741, doi:10.1175/JAM2502.1.
- Brandes, E. A., G. Zhang, and J. Vivekanandan, 2002: Experiments in rainfall estimation with a polarimetric radar in a subtropical environment. *J. Appl. Meteor.*, **41**, 674–685, doi:10.1175/1520-0450(2002)041<0674:EIREWA>2.0.CO;2.
- Chandrasekar, V., V. N. Bringi, S. A. Rutledge, A. Hou, E. Smith, G. S. Jackson, E. Gorgucci, and W. A. Petersen, 2008: Potential role of dual-polarization radar in the validation of satellite precipitation measurements: Rationale and opportunities. *Bull. Amer. Meteor. Soc.*, **89**, 1127–1145, doi:10.1175/2008BAMS2177.1.
- , R. Keranen, S. Lim, and D. Moisseev, 2013: Recent advances in classification of observations from dual polarization weather radars. *Atmos. Res.*, **119**, 97–111, doi:10.1016/j.atmosres.2011.08.014.
- Ciach, G. J., 2003: Local random errors in tipping-bucket rain gauge measurements. *J. Atmos. Oceanic Technol.*, **20**, 752–759, doi:10.1175/1520-0426(2003)20<752:LREITB>2.0.CO;2.
- , and W. F. Krajewski, 2006: Analysis and modeling of spatial correlation structure in small-scale rainfall in central Oklahoma. *Adv. Water Resour.*, **29**, 1450–1463, doi:10.1016/j.advwatres.2005.11.003.
- Cifelli, R., V. Chandrasekar, S. Lim, P. C. Kennedy, Y. Wang, and S. A. Rutledge, 2011: A new dual-polarization radar rainfall algorithm: Application in Colorado precipitation events. *J. Atmos. Oceanic Technol.*, **28**, 352–364, doi:10.1175/2010JTECHA1488.1.
- Cunha, L. K., J. A. Smith, M. L. Baeck, and W. F. Krajewski, 2013: An early performance evaluation of the NEXRAD dual-polarization radar rainfall estimates for urban flood applications. *Wea. Forecasting*, **28**, 1478–1497, doi:10.1175/WAF-D-13-00046.1.
- , —, W. F. Krajewski, M. L. Baeck, and B.-C. Seo, 2015: NEXRAD NWS polarimetric precipitation product evaluation for IFloodS. *J. Hydrometeorol.*, doi:10.1175/JHM-D-14-0148.1, in press.
- Fulker, D., S. Bates, and C. Jacobs, 1997: Unidata: A virtual community sharing resources via technological infrastructure. *Bull. Amer. Meteor. Soc.*, **78**, 457–468, doi:10.1175/1520-0477(1997)078<0457:UAVCSR>2.0.CO;2.
- Fulton, R. A., J. P. Breidenbach, D.-J. Seo, D. A. Miller, and T. O'Bannon, 1998: The WSR-88D rainfall algorithm. *Wea. Forecasting*, **13**, 377–395, doi:10.1175/1520-0434(1998)013<0377:TWRA>2.0.CO;2.
- Giangrande, S. E., and A. V. Ryzhkov, 2008: Estimation of rainfall based on the results of polarimetric echo classification. *J. Appl. Meteor.*, **47**, 2445–2460, doi:10.1175/2008JAMC1753.1.
- Hou, A. Y., and Coauthors, 2014: Global Precipitation Measurement (GPM) Mission. *Bull. Amer. Meteor. Soc.*, **95**, 701–722, doi:10.1175/BAMS-D-13-00164.1.
- Istok, M., and Coauthors, 2009: WSR-88D dual-polarization initial operational capabilities. *25th Conf. on Int. Interactive Information and Processing Systems (IIPS) in Meteorology, Oceanography, and Hydrology*, Phoenix, AZ, Amer. Meteor. Soc., 15.5. [Available online at <http://ams.confex.com/ams/pdfpapers/148927.pdf>.]
- Kelleher, K. E., and Coauthors, 2007: A real-time delivery system for NEXRAD Level II data via the internet. *Bull. Amer. Meteor. Soc.*, **88**, 1045–1057, doi:10.1175/BAMS-88-7-1045.
- Klazura, G. E., and D. S. Kelly, 1995: A comparison of high resolution rainfall accumulation estimates from the WSR-88D precipitation algorithm with rain gage data. Preprints, *27th Conf. on Radar Meteorology*, Vail, CO, Amer. Meteor. Soc., 31–34.
- Krajewski, W. F., G. J. Ciach, and E. Habib, 2003: An analysis of small-scale rainfall variability in different climatic regimes. *Hydrol. Sci. J.*, **48**, 151–162, doi:10.1623/hysj.48.2.151.44694.
- , B. Vignal, B.-C. Seo, and G. Villarini, 2011: Statistical model of the range-dependent error in radar-rainfall estimates due to the vertical profile of reflectivity. *J. Hydrol.*, **402**, 306–316, doi:10.1016/j.jhydrol.2011.03.024.
- , A. Kruger, S. Singh, B.-C. Seo, and J. A. Smith, 2013: Hydro-NEXRAD-2: Real time access to customized radar-rainfall for hydrologic applications. *J. Hydroinf.*, **15**, 580–590, doi:10.2166/hydro.2012.227.

- Lerach, D. G., S. A. Rutledge, C. R. Williams, and R. Cifelli, 2010: Vertical structure of convective systems during NAME 2004. *Mon. Wea. Rev.*, **138**, 1695–1714, doi:10.1175/2009MWR3053.1.
- Lim, S., V. Chandrasekar, and V. N. Bringi, 2005: Hydrometeor classification system using dual-polarization radar measurements: Model improvements and in situ verification. *IEEE Trans. Geosci. Remote Sens.*, **43**, 792–801, doi:10.1109/TGRS.2004.843077.
- Marshall, J. S., and W. McK. Palmer, 1948: The distribution of raindrops with size. *J. Meteor.*, **5**, 165–166, doi:10.1175/1520-0469(1948)005<0165:TDORWS>2.0.CO;2.
- Park, H., A. V. Ryzhkov, D. S. Zrnic, and K.-E. Kim, 2009: The hydrometeor classification algorithm for the polarimetric WSR-88D: Description and application to an MCS. *Wea. Forecasting*, **24**, 730–748, doi:10.1175/2008WAF2222205.1.
- Petersen, W. A., and W. Krajewski, 2013: Status update on the GPM Ground Validation Iowa Flood Studies (IFloodS) field experiment. *Geophysical Research Abstracts*, Vol. 15, Abstract EGU2013-13345. [Available online at <http://meetingorganizer.copernicus.org/EGU2013/EGU2013-13345.pdf>.]
- Ryzhkov, A. V., S. E. Giangrande, and T. J. Schuur, 2005a: Rainfall estimation with a polarimetric prototype of WSR-88D. *J. Appl. Meteor.*, **44**, 502–515, doi:10.1175/JAM2213.1.
- , T. J. Schuur, D. W. Burgess, P. L. Heinselman, S. E. Giangrande, and D. S. Zrnic, 2005b: The joint polarization experiment: Polarimetric rainfall measurements and hydrometeor classification. *Bull. Amer. Meteor. Soc.*, **86**, 809–824, doi:10.1175/BAMS-86-6-809.
- Sachidananda, M., and D. S. Zrnic, 1987: Rain rate estimates from differential polarization measurements. *J. Atmos. Oceanic Technol.*, **4**, 588–598, doi:10.1175/1520-0426(1987)004<0588:RREFDP>2.0.CO;2.
- Schumacher, C., and R. A. Houze Jr., 2000: Comparison of radar data from the TRMM satellite and Kwajalein oceanic validation site. *J. Appl. Meteor.*, **39**, 2151–2164, doi:10.1175/1520-0450(2001)040<2151:CORDFT>2.0.CO;2.
- Seliga, T. A., and V. N. Bringi, 1976: Potential use of radar differential reflectivity measurements at orthogonal polarizations for measuring precipitation. *J. Appl. Meteor.*, **15**, 69–76, doi:10.1175/1520-0450(1976)015<0069:PUORDR>2.0.CO;2.
- Seo, B.-C., W. F. Krajewski, A. Kruger, P. Domaszczynski, J. A. Smith, and M. Steiner, 2011: Radar-rainfall estimation algorithms of Hydro-NEXRAD. *J. Hydroinf.*, **13**, 277–291, doi:10.2166/hydro.2010.003.
- , L. K. Cunha, and W. F. Krajewski, 2013: Uncertainty in radar-rainfall composite and its impact on hydrologic prediction for the eastern Iowa flood of 2008. *Water Resour. Res.*, **49**, 2747–2764, doi:10.1002/wrcr.20244.
- , W. F. Krajewski, L. K. Cunha, B. Dolan, J. A. Smith, S. Rutledge, and W. Petersen, 2014: Comprehensive evaluation of the IFloodS precipitation datasets for hydrologic applications. *Extended Abstracts, Ninth Int. Symp. on Weather Radar and Hydrology*, Washington, D.C., Environmental and Water Resources Institute, 1–49.
- Sherretz, L. A., and D. W. Fulker, 1988: Unidata: Enabling universities to acquire and analyze scientific data. *Bull. Amer. Meteor. Soc.*, **69**, 373–376, doi:10.1175/1520-0477(1988)069<0373:UEUTAA>2.0.CO;2.
- Skofronick-Jackson, G., W. A. Petersen, A. Y. Hou, E. F. Stocher, J. Kaye, and R. Kakar, 2013: Global Precipitation Measurement (GPM) science implementation plan. NASA GSFC Doc., 162 pp. [Available online at <http://pmm.nasa.gov/resources/documents/home>.]
- Steiner, M., and J. A. Smith, 2002: Use of three-dimensional reflectivity structure for automated detection and removal of nonprecipitating echoes in radar data. *J. Atmos. Oceanic Technol.*, **19**, 673–686, doi:10.1175/1520-0426(2002)019<0673:UOTDRS>2.0.CO;2.
- , —, S. J. Burges, C. V. Alonso, and R. W. Darden, 1999: Effect of bias adjustment and rain gauge data quality control on radar rainfall estimation. *Water Resour. Res.*, **35**, 2487–2503, doi:10.1029/1999WR900142.
- Vignal, B., and W. F. Krajewski, 2001: Large-sample evaluation of two methods to correct range-dependent error for WSR-88D rainfall estimates. *J. Hydrometeorol.*, **2**, 490–504, doi:10.1175/1525-7541(2001)002<0490:LSEOTM>2.0.CO;2.
- Villarini, G., W. F. Krajewski, and J. A. Smith, 2009: New paradigm for statistical validation of satellite precipitation estimates: Application to a large sample of the TMPA 0.25° 3-hourly estimates over Oklahoma. *J. Geophys. Res.*, **114**, D12106, doi:10.1029/2008JD011475.
- , B.-C. Seo, F. Serinaldi, and W. F. Krajewski, 2014: Spatial and temporal modeling of radar rainfall uncertainties. *Atmos. Res.*, **135–136**, 91–101, doi:10.1016/j.atmosres.2013.09.007.
- Wang, Y., and V. Chandrasekar, 2009: Algorithm for estimation of the specific differential phase. *J. Atmos. Oceanic Technol.*, **26**, 2565–2578, doi:10.1175/2009JTECHA1358.1.